Nonlinear Behavioral Modeling Dependent on Load Reflection Coefficient Magnitude

Jialin Cai, *Student Member, IEEE*, Justin B. King, *Member, IEEE*, Anding Zhu, *Senior Member, IEEE*, José C. Pedro, *Fellow, IEEE*, and Thomas J. Brazil, *Fellow, IEEE*

***Abstract*—A new frequency-domain nonlinear behavioral modeling technique is presented and validated in this paper. This technique extends existing Padé and poly-harmonic distortion models by including the load reflection magnitude, $|\Gamma_L|$, as a parameter. Although a rigorous approach requires a full 2-D load–pull model to cover the entire Smith chart, simulation and experimental evidence have shown that such a 1-D model—that retains only amplitude information of the load reflection coefficient—can give accuracy close to that of a full 2-D load–pull model. Consequently, neglecting the phase constitutes an approximation that provides large benefits without appearing to lead to a severe compromise in accuracy. Furthermore, compared with traditional load-independent models, the new $|\Gamma_L|$-dependent models provide a major improvement in model accuracy. After a discussion of the model extraction methodology, examples are provided comparing traditional load–pull X-parameter models with the model presented in this paper. The new model not only provides consistently good accuracy, but also has a much smaller model file size. Along with the examples that display the ability of the new modeling technique to predict fundamental frequency behavioral, a second harmonic example is also provided. The modeling approach is also validated using measurements results.**

***Index Terms*—Behavioral model, load–pull model, nonlinear, Padé model, poly-harmonic distortion (PHD) model.**

I. Introduction

NONLINEAR behavioral modeling has been used for device characterization in RF circuit design for many years [1]–[3]. With this kind of model, device performance can be predicted under varying drive and impedance conditions, which allows for the rapid design of complex circuits. Much effort has been devoted to nonlinear behavioral model development at microwave frequencies, resulting in a number of nonlinear behavioral modeling approaches for high-frequency transistors [4]–[17].

The poly-harmonic distortion (PHD) model [4]–[7] (or the basic X-parameter model) has been used successfully to describe nonlinear device behavior around the operating conditions about which it is extracted. It is assumed there is only one large RF signal that must be treated generally, and that the remaining spectral components can be treated as small. This is often the case for power amplifiers (PAs), at least those in "nearly matched" cases [18]. If the device-under-test (DUT) is not perfectly matched at the output port due to a small deviation in load impedance, there will be reflections at the fundamental and the harmonics back into the DUT. These mismatches are considered as small perturbations to simplify the description. The validity of the approximation depends on whether these signals are small enough such that their contributions appear only as linear perturbations.

However, there are several cases of practical importance where it becomes necessary to relax the simplifying approximation just stated, i.e., that the reflected waves depend nonlinearly only on the applied bias conditions and the single large RF incident component at Port 1 at the fundamental frequency [18]–[20]. An example is a bare transistor presented with a very large output mismatch at the fundamental frequency. In this case, the large corresponding fundamental frequency wave at Port 2 will reflect from the mismatch and create a large fundamental incident wave. Both the basic PHD model [4]–[7] and basic Padé model [16], [17] cannot accurately describe the case where the DUT behaves in a fully nonlinear way with respect to large incident waves from both the incident port and the output port [21]. Although extensions such as the quadratic poly-harmonic distortion (QPHD) [4], [5], or the second-order Padé models [16], [17] may help in improving model prediction, inaccuracies still remain. The reduced polynomial (RP) model of [22] has advantages that it has a smaller number of model parameters compared with the PHD model, but not the model accuracy.

To extend the range of validity, an approach using load–pull data in conjunction with the X-parameter model has been shown to work very well [18]–[20]. However, the load–pull-based approach causes pronounced increase in model file size because the model dimensionality is increased by the requirement for additional parameters. Additionally, the extraction of the model requires a secondary signal generator in order to generate the small perturbation signal required during the extraction process [18], thereby increasing the cost and complexity of generating the model.

Another extension from Cardiff University, called the Cardiff model [10]–[13], extends the PHD model to become not only dependent on the large signal on the input side, but also on the output side, which allows the model to include more information, making it more general. However, in order to improve the

This work was supported by the Science Foundation Ireland.

J. Cai, J. B. King, A. Zhu, and T. J. Brazil are with the School of Electrical, Electronic and Communications Engineering University College Dublin (UCD), Dublin 4, Ireland (e-mail: jialin.cai@ucdconnect.ie; justin.king@ucd.ie; anding.zhu@ucd.ie; tom.brazil@ucd.ie).

J. C. Pedro is with the Telecommunications Institute, Universidade de Aveiro, Aveiro 3810-193, Portugal (e-mail: jcpedro@ua.pt).

model accuracy, the traveling waves need to be renormalized to an optimal characteristic impedance different to the one normally used. Moreover, due to the irregular shape of the renormalized data grid, in order to obtain data with the same amplitude of incident wave at the load side, 2-D interpolation has to be used when extracting the model [10], making the model extraction method complex.

In [22], the magnitude of the load reflection coefficient, $|\Gamma_L|$, is introduced within the Padé model for the first time. In this paper, both the QPHD model and the Padé 11/11 model [17] are extended by including the parameter $|\Gamma_L|$. The model derivation procedures are provided, and the extraction method is presented. The results from both simulations and measurements are provided together with a detailed discussion of the issues involved.

This paper is organized as follows. In Section II, the basic theory of the $|\Gamma_{21}|$-dependent models and the model extraction methodology are presented. In Section III, the new modeling technique is validated through both simulation and measurement results. Section IV provides conclusions.

II. Basic Theory of $|\Gamma_{21}|$-Dependent Models

In this section, the theoretical foundations of the load reflection magnitude-dependent model are presented. The quantities we are working with are traveling voltage waves, which are converted from the port voltage, V_n, and the port current, I_n, and n is the port number. The incident waves are called the "A-waves" and the reflected waves are called the "B-waves." For a given DUT, the performance at a specific operating point can be described by the incident and reflected waves at all the different ports and all the different harmonics. This situation is described mathematically in (1) as follows:

$$B_{pm} = F_{pm}\left(A_{11}, A_{12}, \ldots A_{21}, A_{22}, \ldots\right) \tag{1}$$

where F_{pm} is a describing function that associates all of the relevant incident waves A_{qn} with the reflected waves B_{pm}, where p and q range from one to the number of signal ports, and m and n range from zero (dc) to the highest harmonic index.

As the system we describe here is considered to be time invariant, an arbitrary delay to all the input signals, i.e., the incident A-waves, will only result in exactly the same time delay for the output signals, i.e., the shape of the reflected B-waves do not change. Based on this fact, we can normalize the phase of A_{11} so that (1) becomes

$$B_{pm} = F_{pm}(|A_{11}|, A_{12}P^{-2}, \ldots A_{21}P^{-1}, A_{22}P^{-2}, \ldots)P^{+m} \tag{2}$$

where $P = e^{j\emptyset(A_{11})}$.

The reason for normalizing A_{11} can be found in [4]. There are two different approximation methods to simplify (2). The first is based on a Taylor-series approximation and the harmonic superposition principle, which results in the PHD model [4]–[7], while the second is based on Padé approximation and the harmonic superposition principle, which leads to the basic Padé model [16], [17].

The two basic behavioral models just described can give good prediction in the nearly matched case, where we can assume $|\Gamma_{21}| \ll 1$. In this case, the magnitude of A_{21} is small enough such that the spectral linearization of the DUT's response with respect to A_{21} will be valid [18]. Thus, under well-matched conditions, the influence of incident signal A_{21} on the large-signal operating point (LSOP) of the DUT can be considered negligible. Including the dc bias, the LSOP can be expressed as (3)

$$\mathrm{LSOP}_{\mathrm{basic}} = (\mathrm{DC\,bias},\ |A_{11}|). \tag{3}$$

However, as previously mentioned, the PHD model, or the first-order Padé model, cannot readily predict behavior over the entire Smith chart, especially for the operation of bare (unmatched) transistors, or for highly mismatched PAs under strong input drive. In these cases, the nonlinear model functions are more complicated than the case considered in the PHD model and the first-order Padé model. The reason for this is that in the PHD model and first-order Padé model, the large scattered B_{21} wave in both basic models are assumed only to depend on the fundamental input large-signal excitation $|A_{11}|$. However, in the latter highly mismatched cases, the large B_{21} wave, generated by the device in response to the large incident A_{11} wave, will reflect from the mismatch and create a large incident wave, A_{21}, at the output port, also at the fundamental frequency. In the highly mismatched cases, the condition $|\Gamma_{21}| \ll 1$ is no longer satisfied. Thus, for large A_{11}, a large output mismatch means A_{21} can be sufficiently large that it will change the DUT's LSOP, and hence, the spectral approximation used previously becomes invalid [18].

The Cardiff model [10]–[13] can overcome the limitation of the former two basic models by including the amplitude of the large incident wave at the output port, $|A_{21}|$, and the phase difference between the two large incident waves, $\varnothing_{2,1}$, in the LSOP, where $\varnothing_{2,1} = \arg(A_{21}) - \arg(A_{11})$. The LSOP of this model is shown as (4) as follows:

$$\mathrm{LSOP}_{\mathrm{cardiff}} = (\mathrm{DC\,bias},\ |A_{11}|, |A_{21}|, \varnothing_{2,1}). \tag{4}$$

The load–pull X-parameter model provides another choice to solve this problem. In this model, the LSOP not only includes the amplitude of the incident wave $|A_{11}|$, but also the load reflection coefficient Γ_{21}. Hence, the LSOP of the load–pull model becomes (5) as follows:

$$\mathrm{LSOP}_{\mathrm{load\,pull}} = (\mathrm{DC\,bias}, |A_{11}|, \Gamma_{21}). \tag{5}$$

In this paper, a new simpler modeling technique is used to solve the problem. In this modeling technique, the magnitude of the fundamental output load reflection coefficient, $|\Gamma_{21}|$, has been introduced to the model together with $|A_{11}|$. In this way, the large-signal operating area is not localized to a point, but exists around a circle in the Smith chart. This can be viewed as a parameter-controlled large-signal operating circle with $|\Gamma_{21}|$ as the parameter. We name this large-signal operating area the

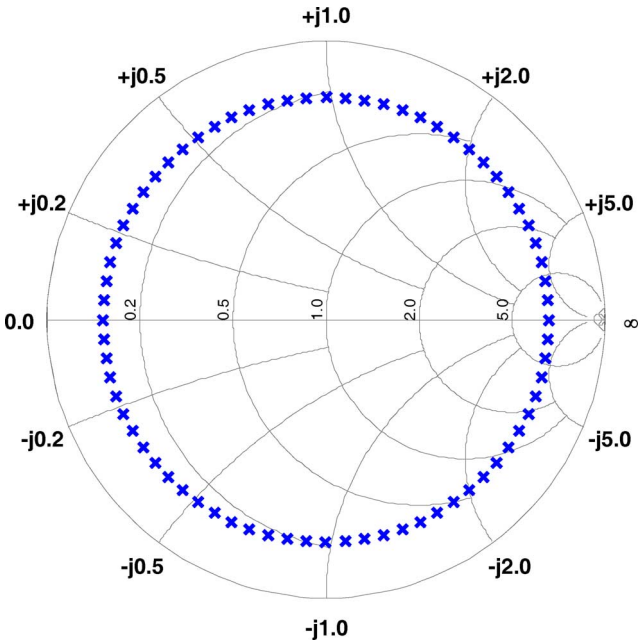

Fig. 1. Smith chart showing load points included in PLSOC when $|\Gamma_{21}|$ is equal to 0.8.

parametric large-signal operating circle (PLSOC), according to (6) as shown follows:

$$\text{PLSOC} = (\text{DC bias}, |A_{11}|, |\Gamma_{21}|). \tag{6}$$

This modeling technique is similar to the load–pull model, but it is not dependent on the phase of the load reflection coefficient. Although a rigorous approach requires a full 2-D load–pull model to cover the entire Smith chart, simulation and experimental evidence have shown that a 1-D load–pull model that retains only the amplitude information can be nearly as accurate as a full 2-D model. Consequently, neglecting the phase constitutes an approximation that provides large benefits without severely compromising accuracy. The DUT's large-signal operating area for each model set is restricted at a load circle on the Smith chart, rather than a specific load point. Take $|\Gamma_{21}|$ equal to 0.8 as an example, the points belonging to this PLOSC are shown in Fig. 1 (72 points along the circle are chosen as an example).

As can be seen from (4) and (5), the LSOP of the Cardiff and load–pull X-parameter models is a steady-state point on the Smith chart; however, in our new modeling technique, the PLSOC is not a point anymore. The nonlinearity of each point in the PLSOC will vary a little bit along this circle, as A_{21} will vary along the PLSOC. Due to this, the accuracy of the model will decrease if we persist with a first-order approximation. In order to retain a high level of accuracy from the model, we extend the basic models to include a second-order term. Thus, we introduce the magnitude of the fundamental output load refection coefficient, $|\Gamma_{21}|$, into the two existing second-order nonlinear behavioral models discussed here, the Padé 11/11 model and the QPHD model.

A. $|\Gamma_{21}|$-Dependent Padé Model

According to [17], aside from the large-signal A_{11}, the output wave B_{pm} depends not only on the incident waves $A_{qn}P^{-n}$, but also the conjugate $(A_{qn}P^{-n})^*$ terms. Thus, (2) can be rewritten as follows:

$$B_{pm} = F'_{pm}(|A_{11}|, A_{qn}P^{-n}, (A_{qn}P^{-n})^*)P^{+m} \tag{7}$$

for all values of q greater than 1 up to the number of signal ports.

Based on the 2-D Padé approximant theory [23], [24], an approximation to $f(x, y)$ around the point (X, Y) can be obtained as

$$\begin{aligned} f(X+\Delta x, Y+\Delta y) &\approx R(X+\Delta x, Y+\Delta y) \\ &= \frac{P(X+\Delta x, Y+\Delta y)}{Q(X+\Delta x, Y+\Delta y)} \\ &= \frac{\sum_{r=0}^{N}\sum_{s=0}^{N'} G_{rs}(X,Y)\Delta x^r \Delta y^s}{\sum_{r=0}^{M}\sum_{s=0}^{M'} H_{rs}(X,Y)\Delta x^r \Delta y^s}. \end{aligned} \tag{8}$$

The LSOP in (7) can be seen as the steady-state point (X, Y), in order to approximate (7), we use Δx and Δy to represent $A_{qn}P^{-n}$ and its conjugate $(A_{qn}P^{-n})^*$. This gives the equivalences

$$\begin{aligned} (X, Y) &\equiv \text{LSOP}_{\text{basic}} \\ \Delta x &\equiv A_{qn}P^{-n} \\ \Delta y &\equiv (A_{qn}P^{-n})^*. \end{aligned} \tag{9}$$

The combination of the Padé approximation and the harmonic superposition principle results in the Padé model. The formulation of the model is provided in [16] and [17], shown in (10) at the bottom of this page.

$$B_{pm} = \frac{G_{pm}(|A_{11}|) + \sum_{qn}\sum_{r}^{N}\sum_{s}^{N'} G_{pm,qn,rs}(|A_{11}|)(A_{qn}P^{-n})^r[(A_{qn}P^{-n})^*]^s}{1 + \sum_{qn}\sum_{r}^{M}\sum_{s}^{M'} H_{pm,qn,rs}(|A_{11}|)(A_{qn}P^{-n})^r[(A_{qn}P^{-n})^*]^s} P^{+m} \tag{10}$$

After the parameter $|\Gamma_{21}|$ has been introduced, the equivalences in (9) become

$$\begin{aligned}(X,Y) &\equiv \mathrm{PLSOC}\\ \Delta x &\equiv A_{qn}P^{-n}\\ \Delta y &\equiv (A_{qn}P^{-n})^{*}.\end{aligned} \tag{11}$$

We then have the $|\Gamma_{21}|$-dependent Padé model, as shown in (12). We choose the Padé 11/11 model as an example in this paper and assume the phase of the large incident signal A_{11} is equal to 0, where (12) can be simplified to (13), shown at the bottom of this page.

B. $|\Gamma_{21}|$-Dependent QPHD Model

A combination of the Taylor series and the harmonic superposition principle results in the PHD model. The formulation of the model is provided in [4] as follows:

$$\begin{aligned}B_{pm} = F_{pm}\left(|A_{11}|\right)P^{m} &+ \sum_{qn} S_{pm,qn}\left(|A_{11}|\right)P^{m-n}A_{qn}\\ &+ \sum_{qn} T_{pm,qn}(|A_{11}|)P^{m+n}A_{qn}^{*}.\end{aligned} \tag{14}$$

After it has been extended to the QPHD model, the resulting expression is

$$\begin{aligned}B_{pm} = F_{pm}\left(|A_{11}|\right)P^{m} &+ \sum_{qn} S_{pm,qn}\left(|A_{11}|\right)P^{m-n}A_{qn}\\ &+ \sum_{qn} T_{pm,qn}\left(|A_{11}|\right)P^{m+n}A_{qn}^{*}\\ &+ \sum_{qn} U_{pm,qn}\left(|A_{11}|\right)P^{m-2n}{A_{qn}}^{2}\\ &+ \sum_{qn} V_{pm,qn}\left(|A_{11}|\right)P^{m+2n}{A_{qn}}^{*2}\\ &+ \sum_{qn} W_{pm,qn}\left(|A_{11}|\right)P^{m}A_{qn}{A_{qn}}^{*}.\end{aligned} \tag{15}$$

In a similar way to the previous case, the $|\Gamma_{21}|$-dependent QPHD model can be obtained by including $|\Gamma_{21}|$,

$$\begin{aligned}B_{pm} = F_{pm}\left(|A_{11}|,|\Gamma_{21}|\right)P^{m} &+ \sum_{qn} S_{pm,qn}\left(|A_{11}|,|\Gamma_{21}|\right)P^{m-n}A_{qn}\\ &+ \sum_{qn} T_{pm,qn}\left(|A_{11}|,|\Gamma_{21}|\right)P^{m+n}A_{qn}^{*}\\ &+ \sum_{qn} U_{pm,qn}\left(|A_{11}|,|\Gamma_{21}|\right)P^{m-2n}{A_{qn}}^{2}\\ &+ \sum_{qn} V_{pm,qn}\left(|A_{11}|,|\Gamma_{21}|\right)P^{m+2n}{A_{qn}}^{*2}\\ &+ \sum_{qn} W_{pm,qn}\left(|A_{11}|,|\Gamma_{21}|\right)P^{m}A_{qn}{A_{qn}}^{*}.\end{aligned} \tag{16}$$

From the expressions of the two new models in (13) and (16), we can see that these new models add no extra complexity apart from including the second-order terms.

C. Model Extraction Methodology

The adopted model extraction procedure can be seen as a least squares problem. Actually, the extraction methodology herein followed is similar to the randomized phase method used in [16] and [17]; the main difference is how we chose the sample points used for model extraction.

In order to explain this methodology, a simple case is chosen as an example. We use the Padé 11/11 model in this example. Assuming the phase of the input large signal is 0, and only taking the fundamental frequency at Port 2 into consideration, (13) will be simplified to (17), shown at the bottom of the following page.

To begin, we keep the magnitude of both the large-signal input $|A_{11}|$, and the fundamental load reflection coefficient, $|\Gamma_{21}|$, unchanged, while the phase of this reflection coefficient is swept. Theoretically, if a model has m parameters, then m independent measurements are sufficient to extract the model. However, in order to reduce errors, we usually take more measurements than needed. Here, each model contains 7 parameters, and 16 measurements are used for each extraction in all the simulation and measurement examples given below.

$$B_{pm} = \frac{G_{pm}\left(|A_{11}|,|\Gamma_{21}|\right)+\sum_{qn}\sum_{r=0}^{N}\sum_{s=0}^{N'} G_{pm,qn,rs}\left(|A_{11}|,|\Gamma_{21}|\right)\left(A_{qn}P^{-n}\right)^{r}\left[\left(A_{qn}P^{-n}\right)^{*}\right]^{s}}{1+\sum_{qn}\sum_{r=0}^{M}\sum_{s=0}^{M'} H_{pm,qn,rs}\left(|A_{11}|,|\Gamma_{21}|\right)\left(A_{qn}P^{-n}\right)^{r}\left[\left(A_{qn}P^{-n}\right)^{*}\right]^{s}}P^{+m} \tag{12}$$

$$B_{pm} = \frac{G_{pm}\left(|A_{11}|,|\Gamma_{21}|\right)+\sum_{qn} G_{pm,qn,10}\left(|A_{11}|,|\Gamma_{21}|\right)A_{qn}+G_{pm,qn,01}\left(|A_{11}|,|\Gamma_{21}|\right)A_{qn}^{*}+G_{pm,qn,11}\left(|A_{11}|,|\Gamma_{21}|\right)A_{qn}A_{qn}^{*}}{1+\sum_{qn} H_{pm,qn,10}\left(|A_{11}|,|\Gamma_{21}|\right)A_{qn}+H_{pm,qn,01}\left(|A_{11}|,|\Gamma_{21}|\right)A_{qn}^{*}+H_{pm,qn,11}\left(|A_{11}|,|\Gamma_{21}|\right)A_{qn}A_{qn}^{*}} \tag{13}$$

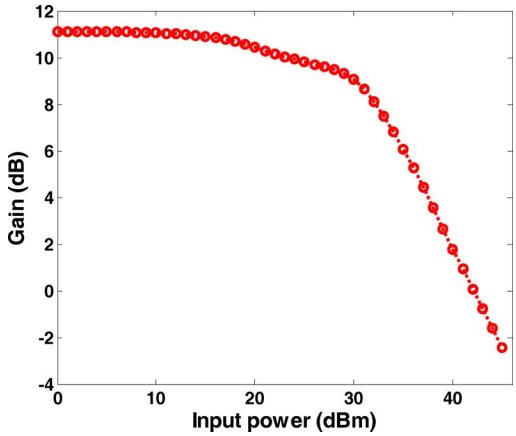

Fig. 2. Simulation curve of Gain versus input power for 45-W GaN at 1 GHz.

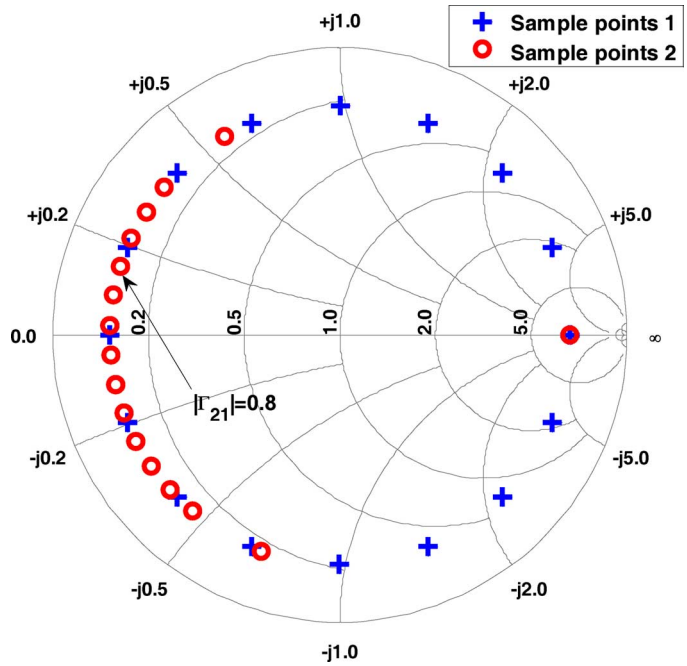

Fig. 3. Reflection coefficient phasors, $|\Gamma_{21}|$, at Port 2.

The amplitude of the incident wave at Port 2 will vary depending on the phase of the load reflection coefficient at that port. This variation results in a similar variation of the operating point around the PLSOC. When the range of this variation range is small, the load sample points may be chosen such that the phase of Γ_{21} is uniformly distributed along the PLSOC. However, when the variation range increases, the situation becomes more complex; if the same method is used in this case, the chosen sample points may not cover the whole range evenly. This makes it difficult for the extracted model to fit the behavior around the entire PLSOC, and the accuracy of the model will degrade.

In order to overcome this problem, an alternative way to choose the sample points is used. As we know, for the simple case described in (17), the operating point of the DUT depends on the amplitude of the incident waves, $|A_{11}|$ and $|A_{21}|$. As $|A_{11}|$ is fixed in each PLSOC, the operating point variation range along the PLSOC depends on the variation range of $|A_{21}|$. Accordingly, we choose the sample points that uniformly distribute the variation of $|A_{21}|$ around the PLSOC.

A simple example is shown here. The DUT is a 45-W GaN transistor (CGH40045F) manufactured by Cree, and its equivalent circuit model was the one supplied by the manufacturer. The device is biased at VGS $= -3$ V and VDS $= 28$ V. Fig. 2 shows the gain-versus-input power curve with the input available power varying from 0 to 45 dBm at 1 GHz, shown in (17) at the bottom of this page.

The selected input power in this example is 41 dBm, at 1 GHz, which corresponds to 10 dB of gain compression. As shown in Fig. 3, the fundamental reflection coefficient, Γ_{21}, is set to a constant amplitude, equal to 0.8.

Two different groups of sample points are used to conduct model extraction so that the accuracy of the extracted models will be compared later. In the first sample group ("Sample points 1"), the chosen load points are evenly distributed along the PLSOC, being the step size of the phase 22.5°; while, in the second group ("Sample points 2"), the sample points are evenly distributed around the variation range of $|A_{21}|$ along the PLSOC. As we can see in Fig. 4, most of the sample points in the first group are distributed in the $|A_{21}|$ range from 2 to 7. Only one point is located in the range from 7 to 11. In the second group, the sample points are evenly distributed along the range of $|A_{21}|$ from 2 to 11.

The difference of the distribution of the two different sample groups results in a significantly different distribution of the fundamental incident waves and reflected waves, A_{21} and B_{21}, at Port 2. Indeed, the corresponding incident and reflected fundamental waves are shown in Figs. 5 and 6. As we can see, sample group 1 lacks the information in zone 1 and zone 2, which sample group 2 has.

After the sample points are taken, we can get the matrix formulation of the problem, shown in (18) at the bottom of the following page, whereby G_{21}, $G_{21,21,10}$, $G_{21,21,01}$, $G_{21,21,11}$, $H_{21,21,10}$, $H_{21,21,01}$, and $H_{21,21,11}$ are the seven parameters of the Padé 11/11 model. This matrix formulation can be represented symbolically as (19)

$$[B] = [A][P]. \tag{19}$$

$$B_{21} = \frac{G_{21}\left(|A_{11}|,|\Gamma_{21}|\right)+G_{21,21,10}\left(|A_{11}|,|\Gamma_{21}|\right)A_{21}+G_{21,21,01}\left(|A_{11}|,|\Gamma_{21}|\right)A_{21}^{*}+G_{21,21,11}\left(|A_{11}|,|\Gamma_{21}|\right)A_{21}A_{21}^{*}}{1+H_{21,21,10}\left(|A_{11}|,|\Gamma_{21}|\right)A_{21}+G_{21,21,01}\left(|A_{11}|,|\Gamma_{21}|\right)A_{21}^{*}+G_{21,21,11}\left(|A_{11}|,|\Gamma_{21}|\right)A_{21}A_{21}^{*}} \tag{17}$$

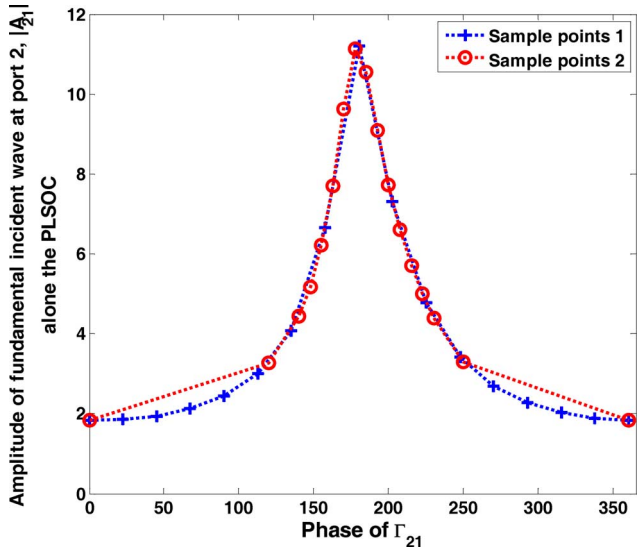

Fig. 4. Distribution of the sample points along the PLSOC based on the amplitude of the incident wave, $|A_{21}|$, at Port 2.

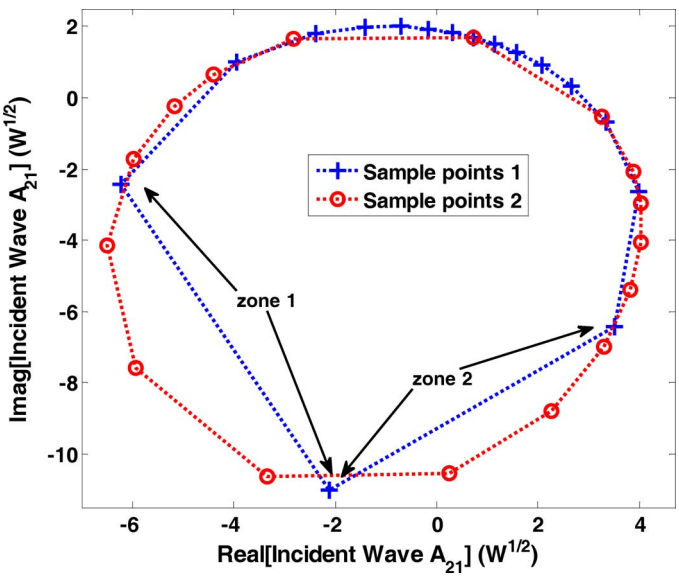

Fig. 5. Incident phasors from two different sample groups, A_{21}, at Port 2.

Since $[A]$ is not square in general, we have to obtain the solution of (19), $[P]$, using its pseudo-inverse, which is constructed by

$$[A]^H[B] = [A]^H[A][P] \tag{20}$$

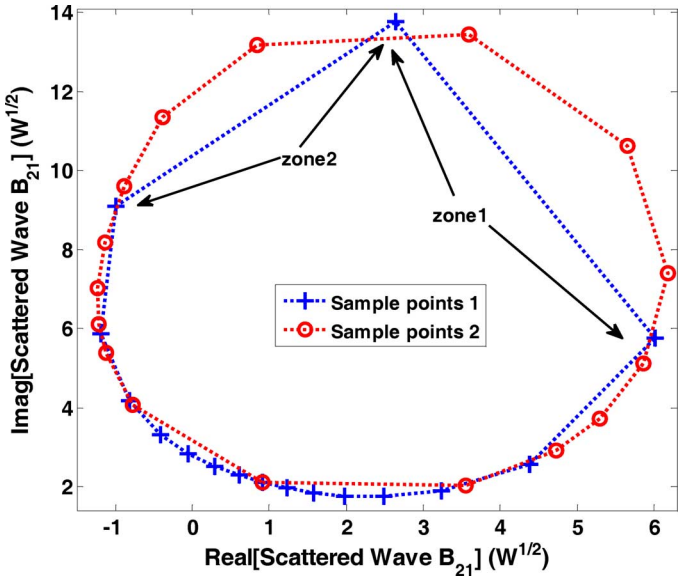

Fig. 6. Scattered fundamental phasors from two different sample groups, B_{21}, at Port 2.

where the superscript H refers to the Hermitian conjugate operation so that

$$[P] = ([A]^H[A])^{-1}[A]^H[B]. \tag{21}$$

Using the above approach, models can be extracted for both sample groups, allowing the comparison between the fundamental output voltage of the two behavioral models, and the circuit model. As we can see in Fig. 7, the Padé 11/11 model extracted from the second sample group provides much better accuracy than the same model extracted from the first sample group. This was to be expected, especially in zone 1 and zone 2. The reason for this is that the points from the second sample group are distributed over the full range of amplitude variation around the PLSOC in a more even fashion than the points from the first sample group. Thus, in strongly nonlinear cases (i.e., cases where the compression level is higher than 3 dB, and $|\Gamma_{21}|$ is larger than 0.5), the second sample group must be used as the appropriate excitation. In other cases, any of the sample groups can be used.

The extraction method presented here can be easily extended to include harmonic frequencies. For example, if the fundamental load condition is fixed, the second harmonic load can be swept, and then a $|\Gamma_{22}|$-dependent model can be extracted. From

$$\begin{bmatrix} B_{21,1} \\ B_{21,2} \\ \vdots \\ B_{21,n} \end{bmatrix} = \begin{bmatrix} 1 & A_{21,1} & A_{21,1}^* & A_{21,1}A_{21,1}^* & -B_{21,1}A_{21,1} & -B_{21,1}A_{21,1}^* & -B_{21,1}A_{21,1}A_{21,1}^* \\ 1 & A_{21,2} & A_{21,2}^* & A_{21,2}A_{21,2}^* & -B_{21,2}A_{21,2} & -B_{21,2}A_{21,2}^* & -B_{21,2}A_{21,2}A_{21,2}^* \\ \vdots & \vdots & \vdots & \vdots & \vdots & \vdots & \vdots \\ 1 & A_{21,n} & A_{21,n}^* & A_{21,n}A_{21,n}^* & -B_{21,n}A_{21,n} & -B_{21,n}A_{21,n}^* & -B_{21,n}A_{21,n}A_{21,n}^* \end{bmatrix} \begin{bmatrix} G_{21} \\ G_{21,21,10} \\ G_{21,21,01} \\ G_{21,21,11} \\ H_{21,21,10} \\ H_{21,21,01} \\ H_{21,21,11} \end{bmatrix} \tag{18}$$

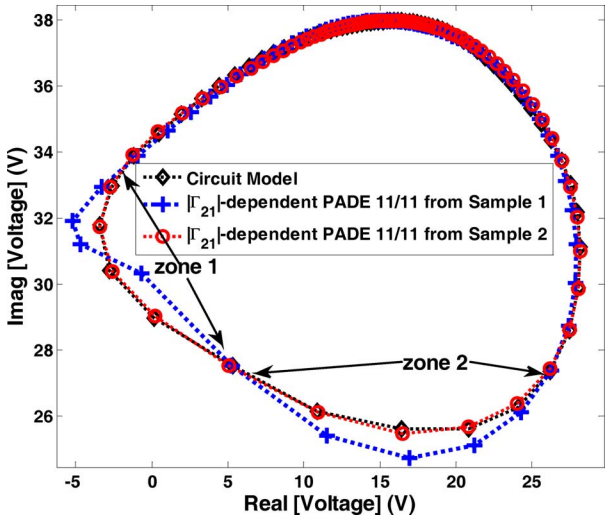

Fig. 7. Simulation results of the two different $|\Gamma_{21}| = 0.8$ load sample groups.

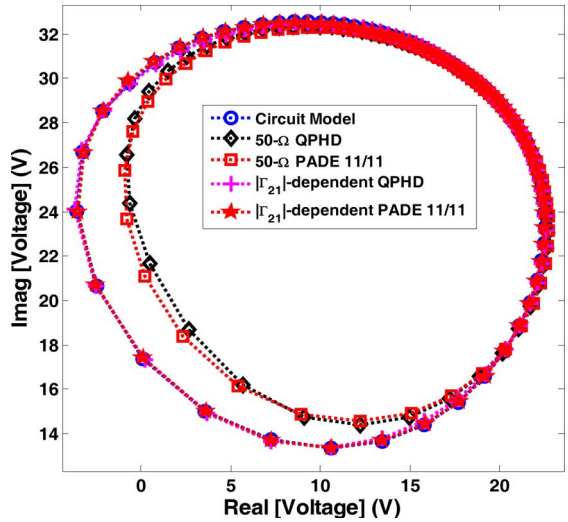

Fig. 8. Simulation results of the $|\Gamma_{21}| = 0.8$ load points group.

the model extraction procedure presented here, we can see that no perturbation signal is required when generating this model, simplifying and reducing the cost of the extraction.

III. Model Validation

In this section, we verify the $|\Gamma_L|$-dependent model through both computer simulations and experimental tests.

The first example provided here is intended to test the accuracy of the $|\Gamma_{21}|$-dependent models extracted at $|\Gamma_{21}| = 0.8$ when compared with the $|\Gamma_{21}|$-independent models. The second example shows the prediction of output power and drain efficiency throughout the entire Smith chart by the new model. Another example has been given to compare the traditional load–pull X-parameter model with the newly presented model, not only in terms of the accuracy of both models, but also the model file size. A second harmonic, $|\Gamma_{22}|$-dependent model simulation result is also provided.

Measurements are then performed on a gallium–nitride (GaN) high electron-mobility transistor (HEMT) and we extract a $|\Gamma_{21}|$-dependent model using the methodology previously described. Comparisons between the models and the measured data are then given and the results are presented.

A. Computer Simulations

We use an equivalent-circuit transistor model in Agilent Technologies' Advanced Design System (ADS) simulation environment in the test. The DUT here is the same as in Section II-C.

The load points in the first example for detailed comparison are the same as shown in Fig. 1. In this group, $|\Gamma_{21}|$ is equal to 0.8, the phase of the reflection coefficients ranges from 0° to 355°, with a step size of 5°, giving 72 points in total. The input power is 32 dBm, at 1 GHz, and 3-dB compression. The device is biased at -3 V for VGS and 28 V for VDS. After model extraction, simulation was performed in MATLAB.

The simulation results are provided in Fig. 8 using the output voltage as a comparison metric. From this figure, we can see that the $|\Gamma_{21}|$-dependent models, both the QPHD model (magenta cross in online version) and Padé 11/11 model (red star in online version), provide much better prediction than the 50-Ω Padé 11/11 model (red square in online verison) and the 50-Ω QPHD model (black diamond) under strong nonlinearity conditions. The results also emphasize that the 50-Ω models are incapable of giving good prediction under strong nonlinearity conditions, even if these models are extended to second order. The detailed relative errors are given in Fig. 9 from which it may be seen that the new $|\Gamma_{21}|$-dependent model provides a major improvement compared to the regular 50-Ω case.

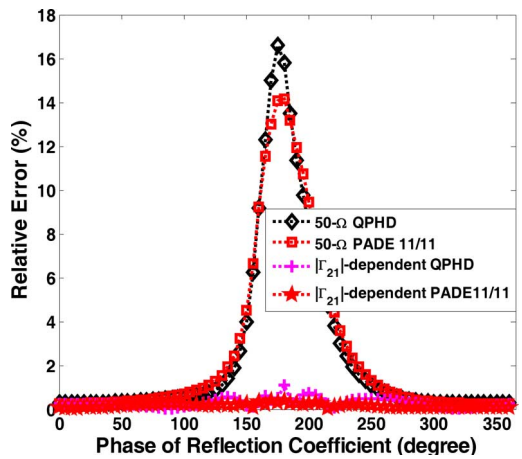

Fig. 9. Relative error (%) of the $|\Gamma_{21}| = 0.8$ load points group with 32-dBm input power at 1 GHz.

Fig. 10 shows the variation of the amplitude of the incident fundamental wave at Port 2, $|A_{21}|$, in the example. From this figure, we can see that the incident wave at Port 2 varies over a wide range, from 1.5 to 6.7. However, even under such a strong nonlinear situation, the new $|\Gamma_{21}|$-dependent models still provide us with good prediction. The combination of the magnitude of load reflection coefficient information, $|\Gamma_{21}|$, with the second-order approximation method, greatly improve the capability of the models in handling significant nonlinearity.

Along with the performance from the example at just a single value of the load reflection coefficient magnitude ($|\Gamma_{21}| = 0.8$) just shown, other examples have been considered.

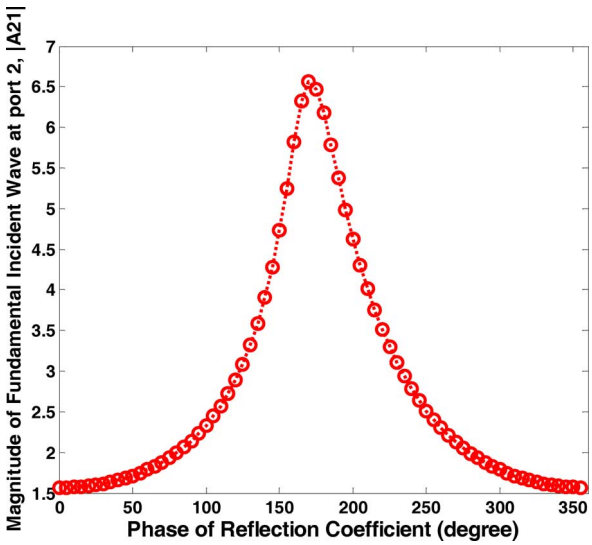

Fig. 10. Amplitude of the incident fundamental wave at Port 2, $|A_{21}|$, at the $|\Gamma_{21}| = 0.8$ load condition with 32-dBm input power at 1 GHz.

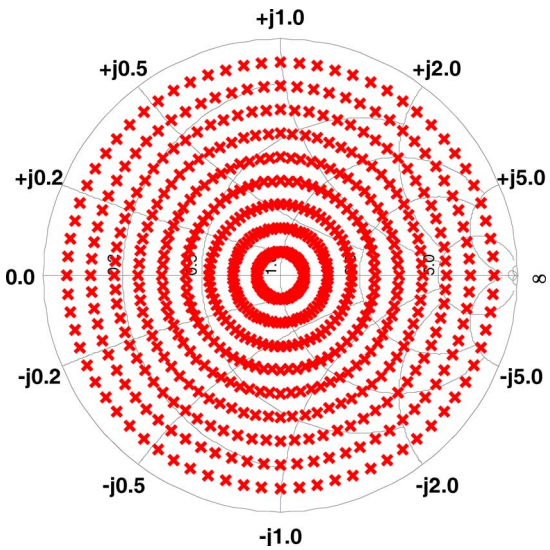

Fig. 11. Smith chart showing load points chosen as an example.

In Fig. 11, the chosen load points for comparison are shown in the Smith chart. In this example, we use the new model to conduct simulations at different load conditions throughout the whole Smith chart. The magnitude of the reflection coefficient ranges from 0.1 to 0.9 with a step size of 0.1; the phase of reflection coefficient ranges from 0° to 355° with a step size of 5°, this gives 648 points in total. In this example, nine sets of $|\Gamma_{21}|$-dependent models are extracted. The model extraction procedure is the same as before. The model we used in this example is a Padé 11/11 model. After models have been extracted, simulations are performed at the load points chosen as shown in Fig. 11.

Fig. 12 demonstrates a comparison between the output power contours using the circuit model and simulation with the $|\Gamma_{21}|$-dependent Padé 11/11 model. From the results, we can see that the new model very closely tracks the results from the circuit model. The output power ranges of these two models are also shown in Table I. From the table we can see

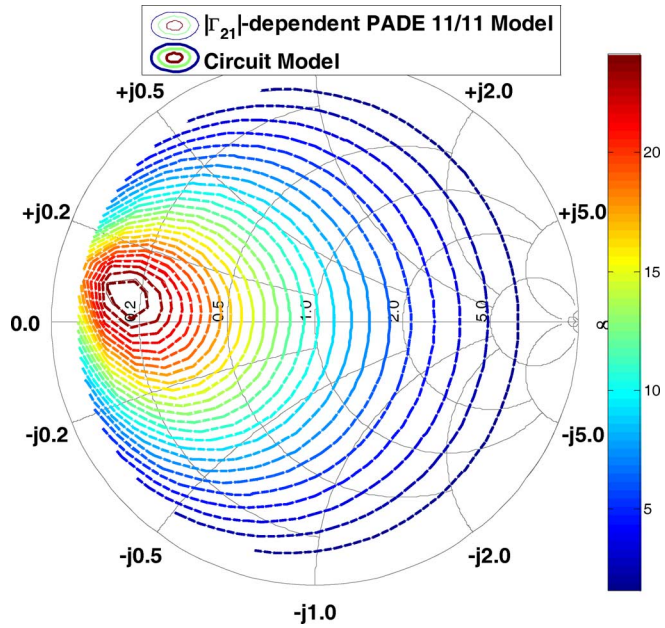

Fig. 12. Output power contours with 32-dBm input power at 1 GHz.

TABLE I
RANGE OF OUTPUT POWER ACROSS SMITH CHART

Model	Output Power Range (W)
Circuit Model	0.6629-25.0610
$\|\Gamma_{21}\|$-dependent Padé 11/11Model	0.6649-24.9985

that the differences between the behavioral model and circuit model results are quite small, showing the good accuracy of the proposed approach.

From the basic theory of the $|\Gamma_{21}|$-dependent model presented in Section II, it is easy to note that this model can be conveniently extended to the dc region. In this example, we also use a dc $|\Gamma_{21}|$-dependent Padé 11/11 model to calculate the dc current. The dc power can then be obtained. After that, a comparison can be made between the drain efficiency contours from circuit model and that from the $|\Gamma_{21}|$-dependent Padé 11/11 model, as shown in Fig. 13.

From the results shown in Fig. 13, we can see that the $|\Gamma_{21}|$-dependent Padé 11/11 model provides as good a prediction of the drain efficiency as it did previously when comparing output power. The drain efficiency ranges of these two models are also shown in Table II. From the figure and the table, we can see that the accuracy of the new behavioral model is very good in terms of the prediction of drain efficiency.

As is well known, both output power and drain efficiency calculations are very important for PA design. Thus, good prediction of these two parameters can provide PA designers a convenient way to produce an accurate design.

Fig. 14 represents a comparison between the circuit model, the $|\Gamma_{21}|$-dependent Padé 11/11 model, and the load–pull X-parameter model. The key difference between a general load–pull model and this new $|\Gamma_{21}|$-dependent model is that the former requires 2-D sweeps throughout the Smith chart, involving both

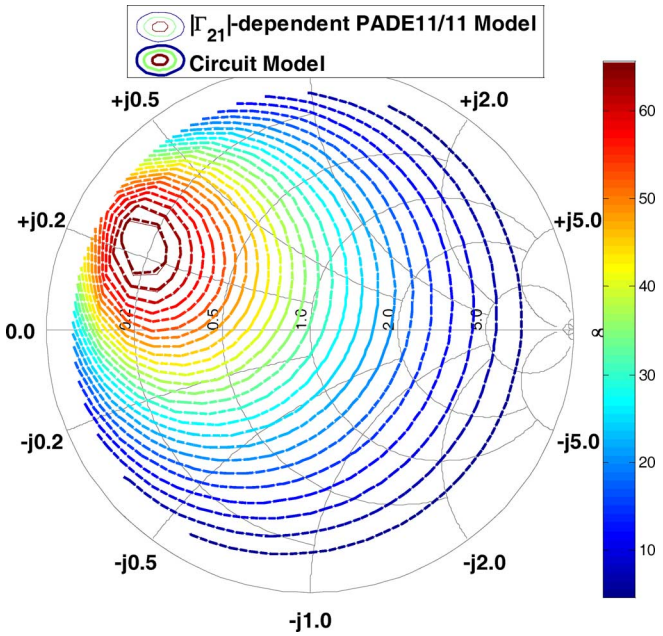

Fig. 13. Output drain efficiency contours with 32-dBm input power at 1 GHz.

TABLE II
RANGE OF DRAIN EFFICIENCY ACROSS SMITH CHART

Model	Drain Efficiency Range (%)
Circuit Model	2.1885-68.1154
$\|\Gamma_{21}\|$-dependent Padé 11/11Model	2.1928-68.0233

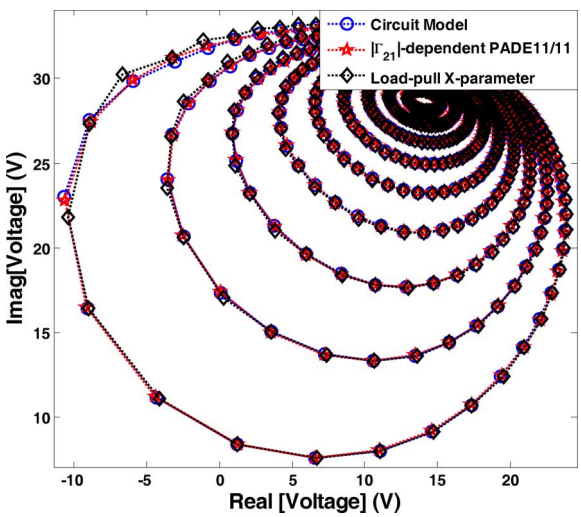

Fig. 14. Simulation results from circuit model, Padé 11/11 model, and load–pull X-parameter model.

the phase and magnitude of the load reflection coefficient, while the latter only needs a 1-D (magnitude) sweep. The comparison metric used here is the fundamental output voltage. The magnitude of the load reflection coefficient in the load–pull X-parameter model varies from 0.1 to 0.9, with a step size of 0.1; the phase of the load reflection coefficient varies from 0° to 350°, with a step size of 10°, giving a total of 324 sets of X-parameters in the load–pull model. The load–pull X-parameter model is directly extracted from equivalent circuit model simulation in

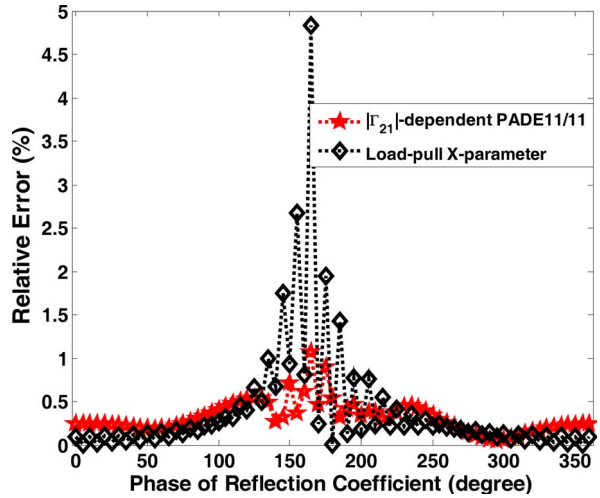

Fig. 15. Relative error (%) of the $|\Gamma_{21}| = 0.9$ load points group with 32-dBm input power at 1 GHz from $|\Gamma_{21}|$-dependent Padé 11/11 model and load–pull X-parameter model.

ADS. The same nine sets of $|\Gamma_{21}|$-dependent Padé 11/11 models are used here, with the magnitude of the reflection coefficient ranging from 0.1 to 0.9. The fundamental frequency and bias condition are the same as before.

Simulation results are shown in Fig. 14. From the figure, we can see that both the $|\Gamma_{21}|$-dependent Padé 11/11 model and the load–pull X-parameter model provide good prediction. However, when compared with the load–pull model, the new $|\Gamma_{21}|$-dependent model still gives better accuracy, especially in the region where the reflection coefficient is high.

A detailed example comparing the accuracy of the load–pull X-parameter model and the $|\Gamma_{21}|$-dependent Padé model is also presented here. We choose the outermost circle of load points as our sample points. In this group, the magnitude of the reflection coefficient is 0.9, the phase of the reflection coefficient ranges from 0° to 355° with a step size of 5°, giving 72 points in total. The relative errors from the two different models are given in Fig. 15. From the figure, it can be seen that both models give good prediction over most of the points, the relative errors being much lower than 1%. However, the accuracy of the load–pull X-parameter model decreases when the phase ranges from 120° to 240°, where the maximum relative error increases to nearly 5%. The reason is that the level of nonlinearity increases when the reflection coefficient enters into this area, and the density of the load–pull model is not high enough to provide sufficient prediction accuracy in this region. If we want to obtain better accuracy, we have to increase the density of the load–pull model. The new $|\Gamma_{21}|$-dependent model provides us with more accurate and more robust prediction throughout all the sample points.

In addition to the comparison of the model simulation results, the parameter count for each model is also compared here. From Table III we can see that the new $|\Gamma_{21}|$-dependent model greatly reduces the number of model parameters, and this will greatly decrease the model file size.

The modeling technique can be easily extended to include the harmonic frequencies, and a multi-harmonic example is also provided here. The same Cree 45-W transistor is used with an input power of 41 dBm—which corresponds to a

TABLE III
PARAMETER NUMBERS FROM DIFFERENT MODELS

Model	Parameter Numbers
Load-pull X-parameter Model	3*9*36
$\|\Gamma_{21}\|$-dependent Padé 11/11Model	7*9

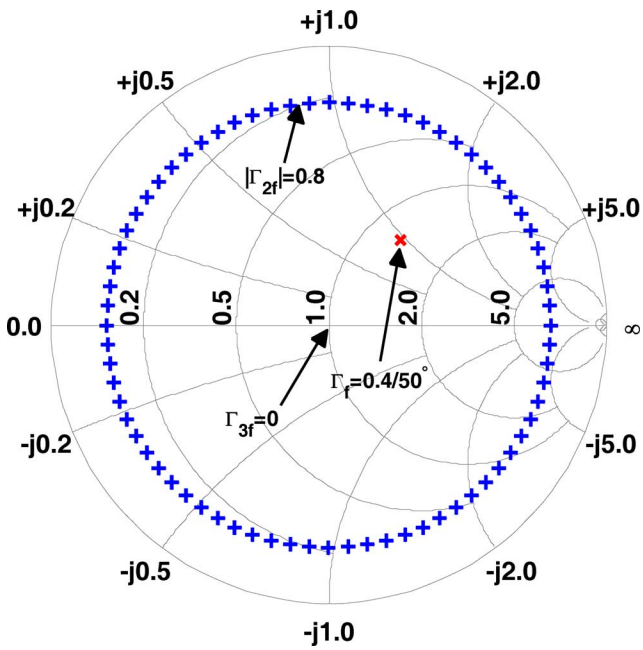

Fig. 16. Smith chart showing second harmonic simulated load points.

10 dB of gain compression—and the bias condition is the same as the former example. The fundamental reflection coefficient $\Gamma_{21} = 0.4\angle 50°$, the magnitude of the second harmonic reflection coefficient, $|\Gamma_{22}|$, equals 0.8, while the reflection coefficients of all remaining harmonics are set to 0. The simulated load points are shown in Fig. 16.

Taking the $|\Gamma_{22}|$-dependent QPHD model as an example, the expression of the reflected second harmonic wave in this case becomes

$$\begin{aligned} B_{22} = & F_{22}\left(|A_{11}|, |\Gamma_{21}|, |\Gamma_{22}|\right) \\ & + S_{22,21}\left(|A_{11}|, |\Gamma_{21}|, |\Gamma_{22}|\right) A_{21} \\ & + T_{22,21}\left(|A_{11}|, |\Gamma_{21}|, |\Gamma_{22}|\right) A_{21}^{*} \\ & + U_{22,21}\left(|A_{11}|, |\Gamma_{21}|, |\Gamma_{22}|\right) A_{21}^{2} \\ & + V_{22,21}\left(|A_{11}|, |\Gamma_{21}|, |\Gamma_{22}|\right) A_{21}^{*2} \\ & + W_{22,21}\left(|A_{11}|, |\Gamma_{21}|, |\Gamma_{22}|\right) A_{21} A_{21}^{*} \\ & + S_{22,22}\left(|A_{11}|, |\Gamma_{21}|, |\Gamma_{22}|\right) A_{22} \\ & + T_{22,22}\left(|A_{11}|, |\Gamma_{21}|, |\Gamma_{22}|\right) A_{22}^{*} \\ & + U_{22,22}\left(|A_{11}|, |\Gamma_{21}|, |\Gamma_{22}|\right) A_{22}^{2} \\ & + V_{22,22}\left(|A_{11}|, |\Gamma_{21}|, |\Gamma_{22}|\right) A_{22}^{*2} \\ & + W_{22,22}\left(|A_{11}|, |\Gamma_{21}|, |\Gamma_{22}|\right) A_{22} A_{22}^{*}. \end{aligned} \quad (22)$$

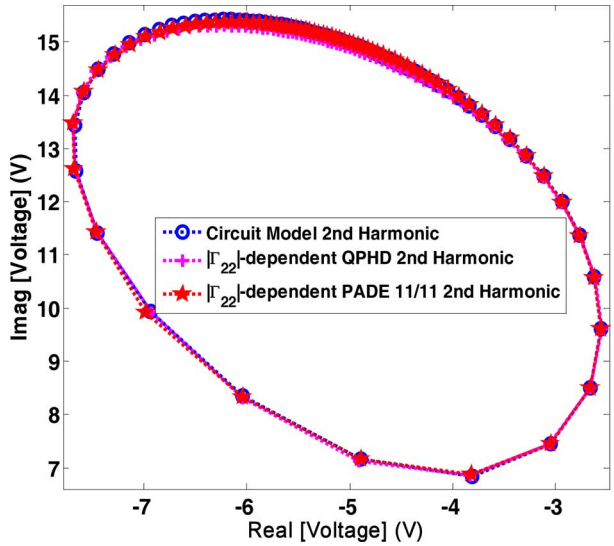

Fig. 17. Simulation results of the $|\Gamma_{22}| = 0.8$ load points group.

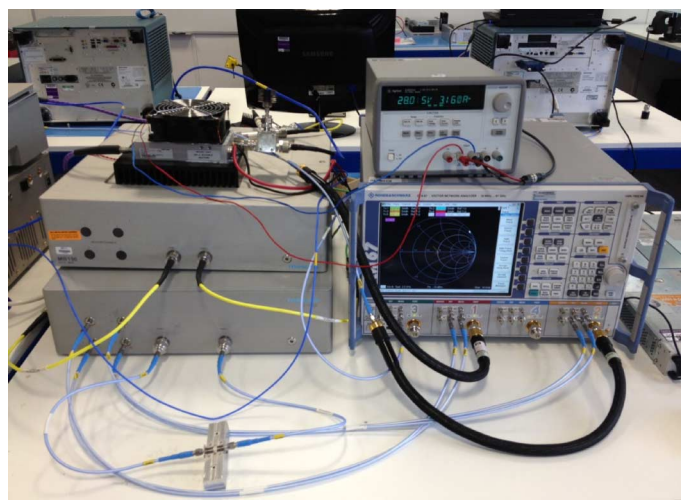

Fig. 18. Mesuro nonlinear measurements system.

The simulation results are shown in Fig. 17. From the figure, we can see that both $|\Gamma_{22}|$-dependent models i.e., the QPHD and PADE 11/11 models, provide us very accurate predictions.

B. Experimental Measurements

Experimental test results are also provided in order to validate the proposed behavioral modeling technique. The Cree GaN 10-W transistor was measured here. The device is operated at 1.5 GHz and excited by a 35-dBm large signal at the input of the device. The gate and drain are biased at -3 and 28 V, respectively. The compression level is 2.8 dB. The test bench used here is a Mesuro nonlinear measurements system, as shown in Fig. 18. In this example, the magnitude of the reflection of the load points chosen is 0.9, and the phase varies around the center point, with 72 points in total.

The results are shown in Fig. 19. The quantity compared here is the fundamental output voltage at Port 2. From the results, we can see that the new models, both the $|\Gamma_{21}|$-dependent Padé 11/11 model (red stars in online version) and the $|\Gamma_{21}|$-dependent QPHD model (magenta cross in online version) provide

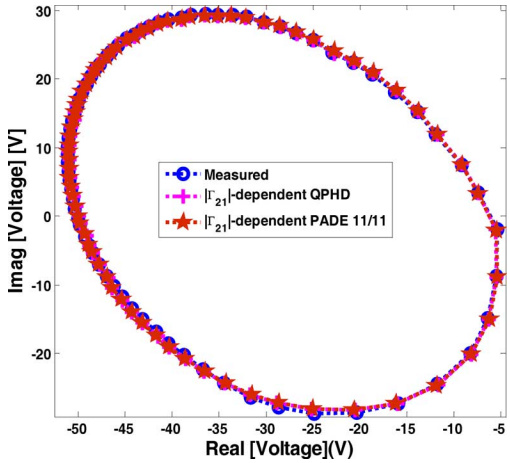

Fig. 19. Measured and modeled results of the $|\Gamma_{21}| = 0.9$ load points from the 10-W transistor.

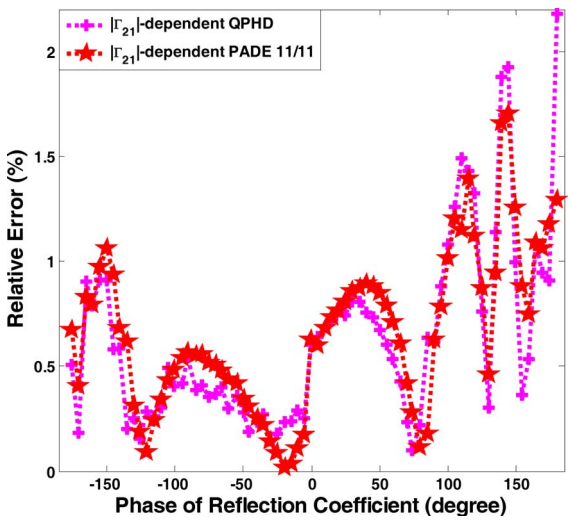

Fig. 20. Relative errors of different modeled results of the $|\Gamma_{21}| = 0.9$ load points.

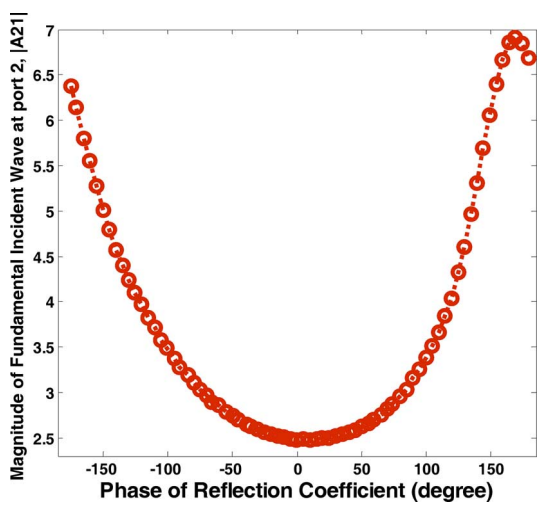

Fig. 21. Amplitude of the incident fundamental wave at Port 2, $|A_{21}|$, at the $|\Gamma_{21}| = 0.9$ load condition with 35-dBm input power at 1.5 GHz.

good prediction, the modeled results matching the measured results very well. Although the magnitudes of the reflection coefficients at the measured points have a small deviation from the specified value of 0.9, the accuracy of the models is still very good, which shows the strong prediction ability of the new modeling technique.

In Fig. 20, the relative errors of the two different $|\Gamma_{21}|$-dependent models are shown. From this figure, we can see that the relative errors are much smaller than 2% both from QPHD model and Padé 11/11 model over most of the chosen points. Fig. 21 shows the amplitude of the incident fundamental wave at Port 2, $|A_{21}|$, at the example load points with 35-dBm input power at 1.5 GHz. From this figure, we can see that the variation of the $|A_{21}|$ is high, approximately from 2.4 to 7, which shows the strong nonlinearity under the chosen load conditions. Even with such strongly nonlinear operation, both models provide us with good prediction, which proves the powerful capability of the new modeling technique in handling strong nonlinearity.

IV. Conclusion

A new frequency-domain $|\Gamma_{21}|$-dependent model has been presented and validated. This new modeling technique can be introduced into both a Padé behavioral model and a PHD model. A simple and efficient model extraction methodology has been provided, reducing the load–pull model from a 2-D sweep to a 1-D sweep. Examples based on the $|\Gamma_{21}|$-dependent Padé and QPHD models, beyond a multi-harmonic example, were also given. The performance of both models has been studied, and both simulated and experimentally measured results showed that the proposed new modeling technique provides high-level and reliable accuracy. Compared with the traditional load–pull X-parameter model, the new modeling technique not only gives better and more consistent accuracy, but also has a much smaller model file size.

References

[1] J. M. Horn *et al.*, "X-parameter measurement and simulation of a GSM handset amplifier," in *Proc. Eur. Microw. Integr. Circuits Conf.*, Amsterdam, The Netherlands, 2008, pp. 135–138.

[2] J. Cai and T. J. Brazil, "X-parameter-based frequency doubler design," in *Proc. Eur. Microw. Conf.*, Amsterdam, The Netherlands, 2012, pp. 1174–1177.

[3] T. S. Nielsen, M. Dieudonne, C. Gillease, and D. E. Root, "Doherty power amplifier design in gallium nitride technology using a nonlinear vector network analyzer and X-parameters," in *Proc. IEEE Compound Semiconduct. Integr. Circuit Symp.*, La Jolla, CA, USA, 2012, pp. 1–4.

[4] J. Verspecht and D. E. Root, "Poly harmonic distortion modeling," *IEEE Microw. Mag.*, vol. 7, no. 3, pp. 44–57, Jun. 2006.

[5] J. Verspecht, "Everything you've always wanted to know about hot S22 (but were afraid to ask)," presented at the IEEE MTT-S Int. Microw. Symp. Introducing New Concepts in Non-linear Netw. Design Workshop, Seattle, WA, USA, 2002.

[6] J. Verspecht, D. Williams, D. Schreurs, K. Remley, and M. D. Mckinley, "Linearization of large-signal scattering functions," *IEEE Trans. Microw. Theory Techn.*, vol. 53, no. 4, pp. 1365–1376, Apr. 2005.

[7] D. E. Root and J. Verspecht, "Broad-band poly-harmonic distortion (PHD) behavioral models from fast automated simulations and large-signal vectorial network measurements," *IEEE Trans. Microw. Theory Techn.*, vol. 53, no. 11, pp. 3656–3664, Nov. 2005.

[8] F. Verbeyst and V. Bossche, "VIOMAP, 16QAM and spectral regrowth: Enhanced prediction and predistortion based on two-tone black-box model extraction," in *Proc. ARFTG Conf. Dig.*, Orlando, FL, USA, Spring, 1995, pp. 19–28.

[9] F. Verbeyst and V. Bossche, "Measurement-based behavioral model under mismatched conditions: A new and easy approach for an accurate model," in *Eur. Microw. Conf.*, 2005, pp. 605–608.

[10] H. Qi, J. Benedikt, and P. J. Tasker, "Nonlinear data utilization: From direct data lookup to behavioral modeling," *IEEE Trans. Microw. Theory Techn.*, vol. 57, no. 6, pp. 1425–1432, Jun. 2009.

[11] S. P. Woodingon *et al.*, "Behavioral model analysis of active harmonic load–pull measurements," in *IEEE MTT-S Int. Microw. Symp. Dig.*, May 2010, pp. 1688–1691.

[12] R. S. Saini *et al.*, "Interpolation and extrapolation capabilities of nonlinear behavioral models," in *Proc. ARFTG Conf.*, Tempe, AZ, USA, 2011, pp. 1–4.

[13] P. J. Tasker and J. Benedikt, "Waveform inspired models and the harmonic balance emulator," *IEEE Microw. Mag.*, vol. 12, no. 2, pp. 38–54, Apr. 2011.

[14] D. E. Root, "Future device modeling trends," *IEEE Trans. Microw. Mag.*, vol. 13, no. 7, pp. 45–59, Nov. 2012.

[15] D. Gunyan, J. Horn, J. Xu, and D. E. Root, "Nonlinear validation of arbitrary load X-parameter and measurement-based device models," in *ARFTG Microw. Meas. Conf.*, Boston, MA, USA, 2009, pp. 1–4.

[16] J. Cai and T. J. Brazil, "Padé-approximation-based behavioral modeling," in *IEEE MTT-S Int. Microw. Symp. Dig.*, Seattle, WA, USA, Jun. 2013, pp. 1–4.

[17] J. Cai, J. King, B. Merrick, and T. J. Brazil, "Padé-approximation-based behavioral modeling," *IEEE Trans. Microw. Theory Techn.*, vol. 61, no. 12, pp. 4418–4427, Dec. 2013.

[18] D. E. Root, J. Verspecht, J. Horn, and M. Marcu, *X-Parameters*. New York, NY, USA: Cambridge Univ. Press, 2013, pp. 112–148.

[19] G. Simpson, J. Horn, D. Gunyan, and D. E. Root, "Load–pull + NVNA = Enhanced$X$-parameters for PA designs with high mismatch and technology-independent large-signal device models," in *Proc. ARFTG Conf.*, Portland, OR, USA, 2008, pp. 88–91.

[20] J. Horn, D. E. Root, and G. Simpson, "GaN device modeling with X-parameters," in *Proc. IEEE Compound Semiconduct. Integr. Circuit Symp.*, Monterey, CA, USA, 2010, pp. 1–4.

[21] J. C. Pedro, "A glimpse on behavioral modeling technology for microwave transistors," in *Proc. 14th Annu. IEEE WAMICON*, Orlando, FL, USA, 2013, pp. 1–6.

[22] J. Cai and T. Brazil, "Reduced-complexity polynomial based nonlinear behavioral modeling," *IEEE Microw. Wireless Compon. Lett.*, vol. 24, no. 7, pp. 496–498, Jul. 2014.

[23] J. Cai, Y. Wang, and T. J. Brazil, "Padé behavioral model depenent on load reflection magnitude," in *IEEE MTT-S Int. Microw. Symp. Dig.*, Tampa, FL, USA, Jun. 2014, pp. 1–4.

[24] C. H. Lutterodt, "A two-dimensional analogue of Padé approximant theory," *J. Phys. A, Math, Nucl. Gen.*, vol. 7, no. 9, pp. 1027–1037, 1974.

[25] G. A. Baker, Jr. and P. G. Morris, *Padé Approximants*, 2nd ed. New York, NY, USA: Cambridge Univ. Press, 1996, pp. 402–414.